Glaucoma Detection in Mobile Phone Retinal Images Based on ADI-GVF Segmentation with EM initialization

Tin Tin Khaing[1], Thayanee Ruennark[2], Pakinee Aimmanee[3], Stanislav Makhanov[4], and Navapol Kanchanaranya[5]

ABSTRACT: The advanced development of mobile phone and retinal lens tech-nology has made fundus imaging more convenient than ever before. In the digital health era, mobile phone fundus photography has evolved into a low-cost alterna-tive to the standard slit-lamp machine. Existing image processing algorithms have a problem with handling retinal images with narrow fields of view and poor-quality taken by a mobile phone. This paper provides a detailed method to enhance the accuracy of our recently proposed scheme, Alternated Deflation-Inflation Gradient Vector Flow model (ADI-GVF), to improve the segmentation of the optic disk (OD) and the optic cup (OC) for glaucoma detection [1]. We integrated the exclu-sion method (EM), a precise algorithm for localizing the OD, with the ADI-GVF algorithm. This work has experimentally proved that it can detect the bound-aries of the OD and OC very precisely, resulting in a very accurate value of the cup-to-disk area ratio (CDAR) for precise glaucoma prescreening. The proposed method has been tested using a mobile phone dataset and two standard datasets (Drishti-GS and HFS). In mobile phone dataset, it obtains TPR up to 93.33%, and FOR as low as 6.66%. Satisfactory rates of TPR and FOR are also reported for those two standard datasets. In addition, the comparison using three datasets shows that the proposed algorithm outperforms other state-of-the-art methods.

Keywords: Glaucoma, Exclusion Method, Iterative GVF, Optic Disk Localization, Optic Disk Segmentation, and Optic Cup Segmentation

DOI: 10.37936/ecti-cit.2021151.227261

Received November 29, 2019; revised June 7, 2020; accepted July 12, 2020; available online January 18, 2021

1. INTRODUCTION

Glaucoma is a group of eye disorders that are characterized by damage to the optic nerve. Glaucoma is classified into several different types, including open-angle (most common) and angle-closure. Open-angle glaucoma occurs when the fluid pressure in an eye increases due to the clogging of drainage, which opens the drainage angle formed by the cornea and iris. Angle-closure glaucoma happens when all angles of drainage are blocked. As a result, the fluid cannot circulate through the eye causing higher pressure. That sudden increase in pressure can damage the optic nerves. The health of these nerves is vital for perfect vision. When the damage worsens, glaucoma can lead to progressive vision loss or complete blindness within a few years. Glaucoma is becoming the second leading cause of blindness among the population of any age, globally. In 2020, the number of glaucomatous

[1,2,3,4]School of ICT, Sirindhorn International Institute of Technology, Thammasat University, Thailand., E-mail: d6022300120@g.siit.tu.ac.th, thayanee.ruen@dome.tu.ac.th, pakinee@siit.tu.ac.th and makhanov@siit.tu.ac.th

[1]Division of Fundamental Engineering, Graduate School of Science and Engineering, Chiba University, Japan.

[5]Department of Ophthalmology, Faculty of Medicine, Thammasat University, Thailand., E-mail: navapolk@gmail.com

The authors would like to thankfully acknowledge the financial support granted by Thai Government Research Fund (contract numbers 33/2560 and 24/2561), National Research Council of Thailand (NRCT) (grant number NRCT5-RSA63010-05) and the Center of Excellence in Biomedical Engineering, Thammasat University, Thailand. We wish to thank the Thammasat Eye Center (TEC) for providing the datasets, ground truths, and for conductive discussions regarding this clinical experiment.

patients is estimated to rise to 80 million, an increase of approximately 20 million from 2010 [2]. The World Health Organization recorded that 6.9 million glaucoma patients suffer vision impairment and blindness [3].

Glaucoma is undiagnosed in nine out of ten affected people worldwide [2]. In general, glaucoma has no warning signs at the early stages. The symptoms are gradual, and thus, a patient may not notice a change in vision until the glaucoma is getting worse. If glaucoma is diagnosed early, vision loss can be avoided. Therefore, it is necessary to get eye exams regularly and proper treatment.

Retinal imaging is a modality that can be applied for glaucoma screening. The rapid development of modern technology allows retinal images to be captured via mobile phones attached with a special portable lens. Fig. 1 shows examples of mobile phones attached to wearable retinal lenses that can be purchased from specific companies. The use of a mobile phone with wearable lenses helps retinal imaging to be less bulky, cheaper, easier, and quicker than the standard machine currently used in hospitals. The cost-effectiveness and convenience of this technology impacts the digital transformation of health services. In the future, the ophthalmologists will be able to handle the large-scale assessment of retinal diseases, including glaucoma.

Fig.1: *Mobile phones attached to retinal lenses. The above images are available from the commercial websites: www.d-eyecare.com, www.peekvision.org, volk.com, and www.welchallyn.com, respectively.*

However, the retinal images acquired from mobile phones attached to wearable lenses often have poor quality. Sometimes, abnormally bright regions, caused by external light during image capture, are present in the image. The vessel structures do not appear perfectly in most images due to the narrow field of view. The low-contrast between the OD and OC regions usually causes the boundary between regions to be blurry. Thus, the images which are taken by mobile phones have poorer quality than those taken by a slit-lamp machine. The characteristics of mobile phone images and abnormalities from the patients lead to a new challenge of automatic glaucoma detection and require an improved algorithm to overcome those difficulties.

Previously, there have been large efforts to analyze the reliability and quality issues of mobile phone retinal images for computer-aided diagnosis systems in ophthalmology. Diabetic retinopathy pre-screening [4] and glaucoma assessment [1][5] are performed by detecting abnormalities in the images acquired by a mobile phone. This work is based on our previously proposed method, Alternated Deflation-Inflation Gradient Vector Flow (ADI-GVF) snakes [1] with a more efficient algorithm for localizing the OD. We estimate the likelihood of having glaucoma for the patient using the segmented OD and OC areas in the retinal images obtained by our improved method. By combining the more powerful localization technique and ADI-GVF, we aim to achieve a more accurate detection rate than in our previous work. Another objective is to help ophthalmologists monitor the treatment of glaucoma.

Glaucoma diagnosis through retinal imaging can be accessed by calculating the cup-to-disk ratio, often referred to the *CDR* [6]. The *cup* refers to the optic cup and the *disk* refers to the optic disk. The optic disk (OD), known as the optic nerve head, represents the entry point for the major blood vessels that supply the retina. It appears as a bright and round (sometimes vertically oval) area in the retinal image. Any abnormalities in the OD are related to specific eye diseases. The optic cup (OC) is a brighter region located at the center of the OD [7]. An eye with a larger OC tends to have a higher risk of glaucoma. Examples of a normal retinal image and a suspected retinal image for glaucoma, which were taken by a mobile phone, are shown in Fig. 2.

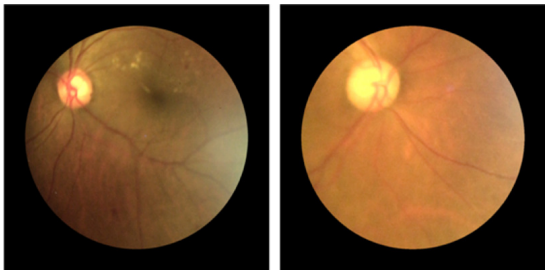

Fig.2: *Retinal images taken by a mobile phone: a normal retina (left) and suspected case of glaucoma (right).*

The CDR can be calculated by several measurement techniques. The commonly used CDRs are vertical CDR (VCDR) and Horizontal CDR (HCDR) [8], as shown in Fig. 3 (a) and (b). The VCDR denotes the ratio of the vertical height of the OC to that of the OD. Likewise, the HCDR denotes the ratio of the horizontal width of the OC to that of the OD. An unhealthy optic nerve causes structural changes in the OC and has an abnormal Neuroretinal Rim (NR) [9]. The NR is the OD area which contains the neural elements: inferior, superior, nasal, and temporal, as shown in Fig. 3 (c). In a healthy retina, the NR tends to be symmetric at the inferior and superior margins

of the OD. If there is an unusual NR, it is a warning sign of glaucoma. Thus, glaucoma can be diagnosed alternatively using the *Inferior Superior Nasal Temporal* (ISNT) rule [10]. The ISNT rule is also called the *neuroretinal rim area rule*. Additionally, there is a variant of CDR computation used for glaucoma assessment, the cup-to-disk area ratio (CDAR). It compares the area of the OC region to that of the OD instead of using the width and the height, as shown in Fig. 3 (d). In our experiment, the probability of having glaucoma is calculated based on the CDAR scheme.

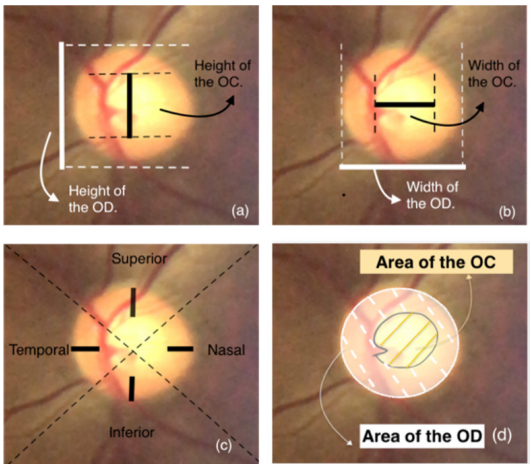

Fig.3: *Representations of VCDR, HCDR, ISNT, and CDAR.*

In this work, we integrated our successful previously proposed technique for optic disk localization together with our previously developed technique for segmentation of regions of an optic cup and an optic disk which had already been tested experimentally to work very well. For the application of glaucoma prescreening, when these two techniques are combined, they considerably enhance the performance of glaucoma prescreening.

2. LITERATURE REVIEW

This section describes the current state-of-the-art methods for localization of the OD, and segmentation of the OD and the OC. Most of the existing methods have been tested using only standard datasets.

2.1 OD Localization

OD localization is the initial step in the process to segment the OD and the OC. Lalonde et al. [11] proposed pyramidal decomposition and template matching to detect the OD. The method creates a pyramid using a Haar-based discrete wavelet transform. Multi-resolution image decomposition is used for providing the aggregated pyramidal candidate OD locations. Moreover, the Canny edge detector is applied to identify edges, and thresholding is performed to build a binary edge map for Hausdorff-based template matching. The Hausdorff distance is computed between two sets of edge points and a circular template in order to find the OD contour. The location with the smallest distance value is considered to be the OD center. Sopharak et al. [12] utilized a median and a contrast-limited adaptive histogram equalization (CLAHE) filter on the intensity image. The entropy value is calculated for each pixel in a local region. The location with the highest entropy value is assumed as the OD candidate. Besenczi et al. [5] combined the works of Lalonde et al. [11] and Sopharak et al. [12] to create a hybrid OD localization process for their work of glaucoma assessment. To localize the OD, our previous method [1] applies the optimal thresholding technique [13] and adaptive histogram equalization. This method finds the regions with the maximum intensity value and merges the nearby regions to get an initial OD region. All of the above methods depend on the features of the OD such as shape, intensity, and entropy. The feature-based methods may be unworkable when the OD's physical appearance becomes abnormal or when other pathological features (severe lesions) appear in the image of an unhealthy retina.

Another subclass of the OD localization methods is based on information of the vascular network. The most cited vessel-based technique, proposed by Hoover and Goldbaum [14], creates a fuzzy segment. An area is generated by voting scores and the corresponding pixels in that area are represented by the fuzzy score of each vessel. Their method produces the points of the strongest convergence as potential OD candidates. Muangnak et al. [15] organized the major vessels into clusters and characterized each point of the image as the shortest distance to those clusters. Their technique, called the vessel transform, is used to detect the OD. Muangnak et al. [16] also provided an improved hybrid OD detection algorithm employing phase portrait analysis. The vessel-based approaches yield high accuracy for OD localization but they suffer from long computational times.

Ultrafast OD localization methods based on the projection of the vascular networks and the gray level intensities onto the horizontal and vertical axes, proposed by Mahfouz and Fahmy [17][18], are approaches which perform well for mobile technology. The technique is called feature projection (FP). FP assumes that the area around the OD contains many vertical vessels and only a few horizontal vessels. The summation of vertical vessel scores at each pixel represents the 1D signal obtained from projecting the vessel features onto the vertical axis. The same process is done horizontally to obtain the 1D signal projected onto the horizontal axis. The largest difference between the vertical and horizontal vessel scores at each pixel defines the horizontal location of the OD. Next, the summation and projection of the image intensi-

ties across the horizontal OD locations can be used to find the maximum, which indicates the vertical location of the OD. Inspired by FP, an extended feature projection (EFP) was presented by Khaing et al. [19]. EFP considers all possible OD locations based on the local maximum of vertical vessels and the local minimum of horizontal vessels, allowing a better chance of getting the correct OD candidates.

2.2 OD Segmentation

The segmentation process of the OD and the OC are important for glaucoma diagnosis for estimating the CDR or CDAR. Almazroa et al. [7] compared the segmentation methods of the disk and the cup, and discussed the challenges faced by the existing algorithms for the identification of glaucoma. Generally, the segmentation techniques are based on the vessel structure, intensity, and edge information.

Muangnak et al. [15-16] integrated their vessel transform and portrait phase algorithms into scale-space analysis so that they are being applied on several resolution levels. Their scale-space segmentation method performs effectively for low-quality images. Joshi et al. [20] proposed a multi-stage strategy to derive a reliable subset of vessel bends at the OD boundary. Bends in a vessel are extracted based on a region of support concept, which automatically chooses the right scale for segmentation. The method is followed by a spline fitting technique to produce the accurate boundary. Cox and Wood [21] proposed an edge detection technique to detect the OD edges. The unconnected edges were then linked by a tracing procedure. Karkuzhali and Manimegalai [22] applied an improved superpixel classification and adaptive mathematical morphology to obtain the OD contour. The method combines neighboring pixels into superpixels and classifies each pixel as the OD or non-OD based on the histogram and center surrounding statistics. Their work was reported as computational-intelligent and compared against k-means and fuzzy c-means.

Giraddi et al. [23] used P-tile thresholding to derive the OD patch. The method assumes the OD area containing the top five percent of the brightest pixels in the retinal images. Then, the too small and too large areas are removed by using connected component analysis to produce the initial patch of OD. To segment the OD boundary, a gradient vector flow (GVF) snake model is derived based on an external force field considered as the diffusion of gradient vectors of the edge map. The method enhances the curve to provide a more accurate OD boundary. It works well even in images which have other pathological structures as exudates. Nonetheless, the method may fail in poor-quality images. Kusumandari et al. [24] presented a comparison of GVF snakes and the ellipse-fitting method in detecting the OD. They concluded that the GVF gives better accuracy than the ellipse-fitting method.

Khan et al. [25] performed local adaptive thresholding and a region growing method to detect the boundary of OD. The method creates an initial seed by searching for the center of the localized OD. The difference between the initial seed and an intensity value of each pixel is measured using a similarity index. The pixel with the smallest difference is added to the initial OD region. The process terminates when the intensity difference between the region and a new pixel is greater than the specified threshold value. Although the region growing model can detect a weak contour, the segmentation result is highly sensitive to the initial contour.

Siddalingaswamy and Prabhu [13] employed iterative thresholding followed by connected component analysis to localize the OD center. The optimal threshold value is calculated based on the intensity value of the image. The OD regions are assumed to be any region which contains pixels with the highest intensity. To obtain the boundary of OD, the implicit active contour model is applied. The energy functional formula is minimized by the use of the gradient and intensity information. Khaing et al. [19] also utilized the active contour method to segment the OD boundary. In general, the active contour approach performs well in high resolution, and high contrast images. However, it fails in some images which have low-contrast between the OD and the background.

2.3 OC Segmentation

Many techniques segment the OC region using the intensity since the OC appears as the brightest region located inside the OD. It is more challenging than the OD segmentation due to presence of high-density vessels around the cup boundary. The region growing [26] and watershed transform method [27] are superb techniques for segmentation of the OC. To detect the cup boundary, Das et al. [26] integrated the segmented results of OC from the region growing and watershed transformation techniques using the logical-OR operation. A circular approximation is applied to fit the final OC contour. Although the methods are simple and computationally efficient, over-segmentation of the OC can occur when the boundaries of the OD and the OC have low-contrast. Karkuzhali and Manimegalai [22] compared the improved superpixel classification (ISPC) technique with the adaptive mathematical morphology (AMM) method. The AMM method detects the OC rim using a sequence of erosion and dilation operations together with adaptive thresholding. They concluded that ISPC outperformed the AMM method in performance and efficiency of computing time. Joshi et al. [20] and Wong et al. [28] made use of a new approach based on bending of small vessels, called kinks. The kinks are generated by the analysis of detected vessel edges within the OD. Then, those kinks

are used to detect the cup area. The kink method performed well for images with clear and strong vessels. It can fail to detect the OC for images with no vessel bends.

Recently, a variant of GVF, *Alternated Deflation-Inflation Gradient Vector Flow snakes* (ADI-GVF), was proposed by Ruennak et al. [1] to segment the boundaries of OD and OC for prescreening glaucoma. The method iteratively alternates the processes of deflating and inflating the GVF until the region converges. In that work, the initial seed of ADI-GVF is obtained by using adaptive thresholding of intensity. ADI-GVF usually gets satisfactory accuracies for the segmentation of both the OD and OC, and for glaucoma prescreening. However, it fails in some cases that are rooted in incorrect initialization. The wrong initialization in those cases is due to uneven lighting in the retinal images acquired from a mobile phone.

In this work, we improve the accuracy of glaucoma prescreening by improving OD and OC segmentation. This is done by integrating the exclusion method (EM) [32], which relies on retinal vessels rather than (solely) intensity to improve OD localization, with the ADI-GVF method. The ADI-GVF method is applied based on the OD location obtained from the EM to segment the OD and the OC.

2.4 Glaucoma Classification

The CDR and the ISNT rules are the commonly used diagnosis parameters used for the indication of glaucoma. To improve detection accuracy, Das et al. [26] made use of a combined evaluation technique using the CDR and ISNT rules. The XOR operation is applied to extract the NR region from the OD and the OC areas. If there is thinning in the superior and inferior rims, which means the violation of the ISNT rule and the CDR exceeds the normal ratio, it indicates the sign of glaucoma. They tested their proposed methods on four standard datasets: high resolution fundus dataset, MESSIDOR, DRIONS-DB and DIARET-DB1. They claimed a high sensitivity of 92.59% for glaucoma detection.

Karkuzhali and Manimegalai [22] developed a decision-support system based on three indicators: the CDR, the ISNT rule, and distance between optic disk center and optic nerve head (DOO). The images are classified as normal or glaucoma using appropriate classifiers and statistical features such as the CDR (<0.3, >0.3), the ISNT rule (low/high), and the DOO (low/high). They reported the best classification accuracy for standard datasets such as DRIVE, DIARETDB0, DIARETDB1, and DRISHTI.

Machine learning techniques have also been applied for glaucoma detection. Chen et al. [29][30] proposed feature learning in detection of glaucoma based on a deep learning technique. Contextualizing training strategy is utilized to generate a hierarchical representation of the retinal images for glaucoma classification. The method extracts the OD area by using the template matching technique. Then, each image containing the segmented OD area is down sampled and used as the input to their proposed convolutional neural network (CNN) to get the cup region. They tested the method on the ORIGA and SCES datasets and evaluated the accuracy of detection using the area under curve (AUC). They obtained glaucoma detection accuracy of up to 89.8%. Li et al. [31] recently proposed a deep learning method named AG-CNN to detect glaucoma and to localize the pathological area. The model comprises the subnets of attention prediction, pathological area localization, and glaucoma classification. Based upon the predicted attention maps, glaucoma detection is done using the deep features provided by the visualized maps of pathological areas. They tested their method on the LAG and RIM-ONE datasets and evaluated their method using AUC. Their proposed AG-CNN outperforms other comparative glaucoma detection methods and achieved up to 97.5% accuracy on the LAG database.

In this work, we use the CDAR scheme for glaucoma classification, thus the OD and OC segmentation results are important. Since deviations of OD and OC areas can mislead the estimation of glaucoma, more robust and effective segmentation algorithms are required to generate accurate ratios. All of the state-of-the-art methods are designated for the standard retinal datasets. Thus, there is a lack of an effective glaucoma assessment technique for poor quality retinal images acquired from mobile cameras.

3. METHODOLOGY

This work presents a method for pre-screening glaucoma by using a vessel-based OD detection technique (EM) and ADI-GVF snakes to segment the OD and the OC. The overall process of detecting glaucoma is depicted in Fig. 4. To localize the OD, the EM is applied based on the extracted vessels. The ADI-GVF method takes the location returned by the EM to segment the boundaries of the OD and the OC. The images are then classified as glaucomatous or non-glaucomatous based on the OD and OC regions. The details of each step are explained next.

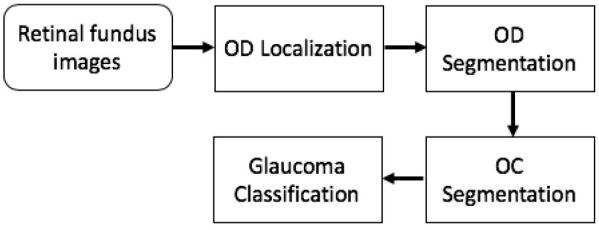

Fig.4: *Flowchart of the proposed method.*

3.1 OD Localization using EM

The green channel of the input image is used to create a grayscale image, as shown in (a) from Fig. 5. The black-top-hat transformation is applied using the cross-shaped structuring element with the size of the maximum thickness of the main retinal vessels. Then, the Otsu thresholding technique is performed to create a binary vessel image (Fig. 5 (b)). The main vertical and horizontal vessel images characterized the skeleton of the vascular network essential for the EM localization algorithm are constructed from the vessel image. We extract the vertical vessel image (Fig. 5 (c)) by performing the morphological opening operation with a linear structuring element, with the size of the maximum vessel thickness. Next, we extract the horizontal vessel image (Fig. 5 (d)) in a similar way.

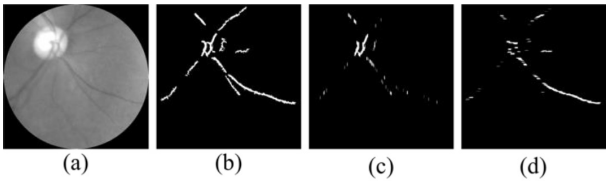

Fig.5: *Process of vessel extraction, (a) grayscale image, (b) vessel image, (c) vertical vessel image, and (d) horizontal vessel image.*

The exclusion method (EM) [32] generalizes the idea proposed by Mahfouz et al. [17][18] that the area around the OD has a low frequency of horizontal vessels and a high frequency of vertical vessels. The EM model is simple and fast. Importantly, the EM is less dependent on the appearance of the OD region. Furthermore, the EM can still work efficiently even when the OD deteriorates, such as changing the size and shape of the image, or when the image contains other lesions such as exudates or hemorrhages.

First, the EM considers all regions along the y-axis that have a frequency function of horizontal vessel pixels that is less than the average of the frequency function. In a similar manner for the x-location, it considers all regions along the x-axis that have a frequency function of vertical vessel pixels that is greater than the average of the frequency function.

Equations (1) and (2) show the mathematical formulas of the OD candidate selection by the EM.

$$y_{loc} = \{y | HV(y) < \overline{HV}\} \tag{1}$$

$$x_{loc} = \{x | VV(x) < \overline{VV}\} \tag{2}$$

HV is a frequency function of horizontal vessel pixels and $\overline{HV}$ is the average of the function HV in the range of y. VV is a frequency function of vertical vessel pixels and $\overline{VV}$ is the average of the function VV in the domain of x. The OD candidates' locations are all (x, y) coordinates such that $x \in xloc$ and $y \in yloc$. The process is illustrated in Fig. 6.

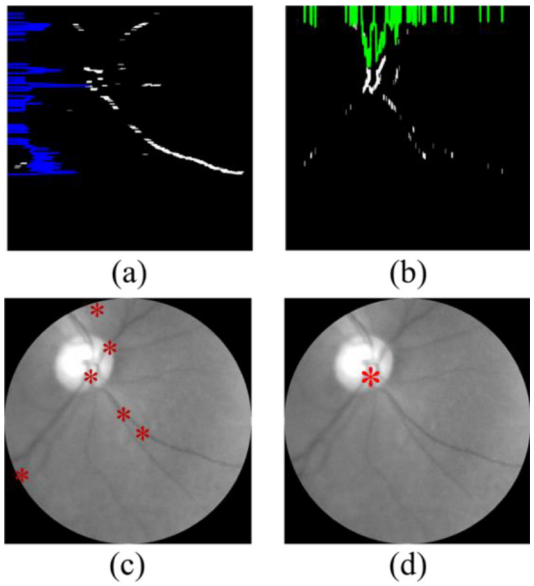

Fig.6: *Process of EM: (a) The HV frequency function of the horizontal vessel image shown in the blue graph, (b) The VV frequency function of the vertical vessel image shown in the green graph, (c) OD candidates from HV and VV, and (d) A final OD location, obtained from the decision tree.*

Since the EM can produce many OD candidates, a decision tree is used to classify a final OD location. We generate a circular region centered at each OD candidate where the radius equals one-twelfth of the width of the image. Then, we extract the following features: number of vessels, area of vessels, vessel thickness, and brightness within the circular region. These features are used to build the decision tree. If there is more than one OD location obtained from the classification process, the decision tree selects the OD location that has the highest number of vertical vessels.

3.2 OD and OC Segmentation

After getting an initial OD location from EM, the regions of OD and OC are detected by applying our previously proposed method, *Alternated Deflation-Inflation Gradient Vector Flow model (ADI-GVF)* [1]. The ADI-GVF model is a variant of the traditional Gradient Vector Flow (GVF). The traditional GVF uses the energy function to find the object boundary. The energy function is the combination of the internal and external forces. It is mathematically defined in Equations (3-8). Firstly, an initial curve or a snake is created. The curve is deformed towards the boundary of the object by the energy function. Then it stops at the point of the minimum energy function.

Let $v(s) = [x(s), y(s)]$ be an initial curve where $s \in [0, 1]$. The energy function is described as

$$E_{snake} = \int_0^1 E_{int} + E_{ext} ds \tag{3}$$

$$\begin{aligned} E_{int} &= E_{elastic} + E_{bending} \\ &= \frac{1}{2}(\alpha|v'(s)|^2 + \beta|v''(s)|^2) \end{aligned} \tag{4}$$

where E_{snake} and E_{int} represent the energy function of the snake and the internal energy which determines the smoothness of the curve. α and β indicate the weighting parameters that are used to define the elasticity and rigidity levels of a snake, respectively. $v'(s)$ and $v''(s)$ denote the first and the second derivatives of $v(s)$ with respect to s.

let $g = g(x)$ be a GVF field, defined as a vector field.

$$E_{ext} = E_{GVF} + E_{Balloon} \tag{5}$$

$$E_{GVF} = \int\int \mu|\nabla g|^2 + |\nabla f|^2|g - \nabla|^2 dxdy \tag{6}$$

$$f(x,y) = -|\nabla(G_\sigma(x,y) * I(x,y))|^2 \tag{7}$$

$$E_{Balloon} = kn \tag{8}$$

where E_{ext}, E_{GVF} and $E_{Balloon}$ represent the external energy containing the GVF and balloon forces, the GVF force which is generated from the diffusion of the gradient vector of the edge map generated from the image, and the balloon forces that are used to perform the inflation or deflation of the curve, respectively. The edge mapping function $f(x,y)$ produces the edge map $f \cdot G_\sigma(x,y)$ and $I(x,y)$ represent a Gaussian function with standard deviation σ and the gray-scale input image. ∇ denotes the gradient operator, μ denotes a smoothness regularization parameter, k denotes the force strength, and n denotes the unit vector normal to the curve at $v(s)$. The sign of k in Eq. (8) controls the curve direction of the GVF model. The inflation process will be performed when k is positive. Otherwise, the deflation process will be performed.

The ADI-GVF model was proposed to overcome the unclear boundary between the OD and the OC, especially in a mobile phone retinal image. It works by repeatedly alternating the processes of deflating and inflating the GVF snake until the region converges. The ADI-GVF algorithm [1] is shown in Fig. 7.

Fig. 8 shows how the ADI-GVF snakes work iteratively for OD segmentation. Fig. 9 illustrates the similar way that ADI-GVF snakes work for OC segmentation.

Algorithm: ADI-GVF

```
Input: IC = initial contour
Output: C

delta = a large number
t = 0.2*Area(IC)
deflat = true

while delta > t
  if deflat == true
      C = GVF applied to IC with a deflation force
  else
      C = GVF applied to IC with an inflation force
  endif

  t = 0.2*Area(IC)
  delta = abs(Area(C) - Area(IC))
  IC = C
  deflat = !deflat

endwhile
```

Fig.7: *ADI-GVF algorithm [1].*

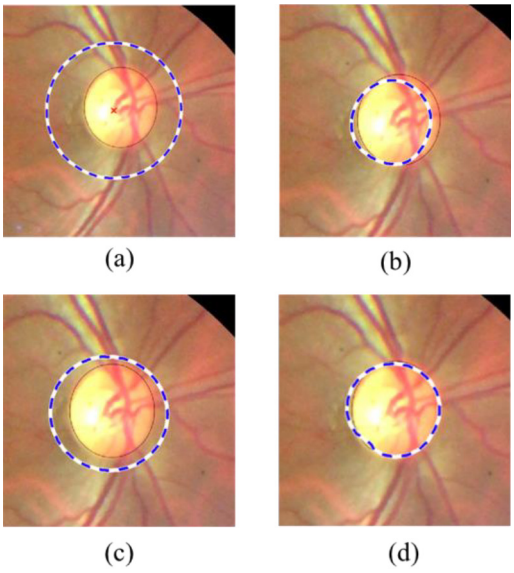

Fig.8: *Illustration of OD segmentation using ADI-GVF, (a) The curve is initially created as a circle with a radius greater than one-sixth of the retinal width and centered at the OD location, obtained from the EM method, (b) After the first iteration, (c) After the second iteration, and (d) the final OD contour after ADI-GVF finishes all iterations.*

The ADI-GVF method may not work well for an OC which sometimes has a concave shape. To solve this problem, histogram equalization is applied to cluster only the high intensity pixels. Fig. 10 shows the OC segmentation results before and after applying the refinement step.

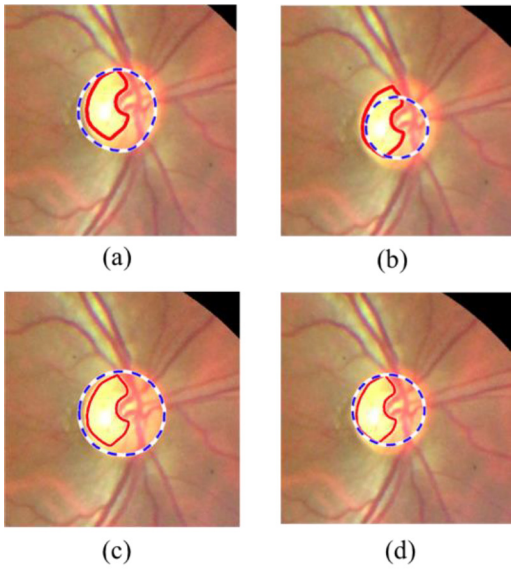

Fig.9: *OC segmentation using ADI-GVF, blue dotted contour - ADI-GVF and the red solid - ground truth, (a) Initial contour set to the OD boundary, (b) After the first iteration, (c) After the second iteration, and (d) the final OC contour after ADI-GVF finishes all iterations.*

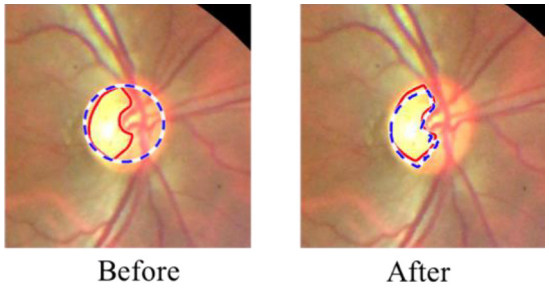

Fig.10: *Correction of OC boundary, before and after the refinement, red solid line - the ground truth and dashed line - the boundary of the OC detected by ADI-GVF.*

3.3 Glaucoma Classification

There have been various attempts to find a useful CDR cutoff value to classify ODs as the glaucomatous or normal. The classification cutoff based on the CDR formula is suggested by Marjanovic [33], as follows. To detect the signs of glaucoma, the cutoff difference is set to be between 0.3 and 0.5. A cutoff of 0.3 indicates the mild stage of glaucoma, whereas 0.5 is used to signify a moderate stage. Several studies show that a cutoff of 0.5 gives high accuracy of glaucoma detection. Hence, the recommended cutoff for more accurate classification in the CDR formula is 0.5. A CDR cutoff 0.5 is equal to a CDAR cutoff of 0.3 which is used in our experiment. Equation 9 shows the derivation of the 0.3 (cutoff) of the CDR formula.

$$CDAR = \frac{Area(OC)}{Area(OD)} = (CDR)^2 < 0.5^2 < 0.3 \quad (9)$$

In this work, a cutoff of 0.3 is used to separate the glaucomatous and normal images.

4. EXPERIMENT, RESULTS & DISCUSSION

In this experiment, we evaluated our proposed method on three datasets. The primary dataset is the retinal dataset which was acquired with a mobile phone attached to a retinal wearable lens. It is comprised of 49 healthy images and 45 glaucomatous images. The fundus images were captured by an iPhone 6 mounted with a volk iNview camera [34] from patients in the Eye Center of Thammasat Chalermprakiat hospital. Ground truth of regions of the optic cup and the optic disk for the positive and the negative cases of glaucoma were also provided by the ophthalmologists from the Eye Center of Thammasat Chalermprakiat hospital. The dimensions of the images are 1,196 × 1,196 in JPG format with a 50-degree field of view. Two other datasets are available publicly for glaucoma assessment. First, the Drishti-GS dataset has 101 retinal images, consisting of 31 normal images and 70 glaucomatous images. It was collected from patients between 40-80 years of age by the Aravind eye hospital [35]. The images were captured centered at the OD with 30-degree field of view. The High-Resolution Fundus (HFS) dataset was publicly provided by a collaborative research group [36]. It contains 15 normal images and 15 glaucomatous images. The dimensions of images in the Drishti-GS and HFS datasets are set to 875 × 1024 and 584 × 876 respectively.

Our system is implemented using MATLAB and run on a MacBook Pro (@2.3 GHz, Dual-Core Intel Core i5). The quality of the mobile phone retinal images, in comparison to those obtained from the slit-lamp standard machine, is normally poor. For instance, an image may have low contrast, faint colors of the optic disk and optic cup, blurry edges, and an uneven background. It may show an incomplete OD and usually has a burst of external light in the retinal areas or shadow. Those problems are depicted in Fig. 11.

There are three main tasks in our algorithm for glaucoma detection: OD localization, OD detection, and OC detection. We evaluate the performance of each task separately and report the example results from each step. The results are evaluated using the annotated ground truths from the ophthalmologist.

4.1 OD Localization

For the OD localization, the accuracy of the EM is compared against the Feature Projection (FP)

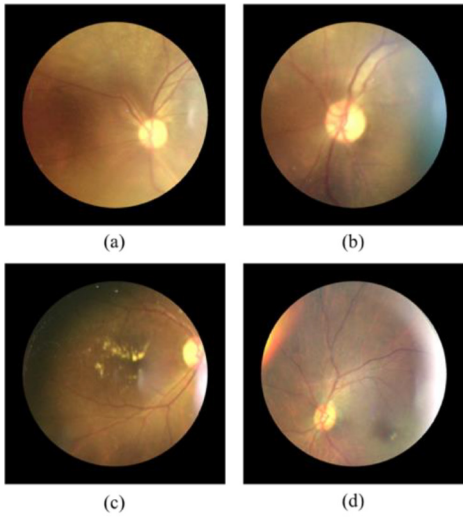

Fig.11: *Examples of poor retinal images.*

method proposed by Mahfouz and Fahmy [18], the Extended Feature Projection (EFP) method [19], and the adaptive thresholding method [1]. To evaluate the OD localization, the location is considered "correct" if it locates the OD inside the ground truth contour of the OD. Fig. 12 shows the qualitative results of the comparative methods obtained from the mobile phone dataset. The black contour represents the ground truth of the OD boundary. The blue cross symbol represents the result obtained from each method.

Table 1 shows the information of each dataset and a comparison of the accuracies of OD localization resulted by the above methods. The EM method works correctly in all cases, and thus obtains 100% accuracy for all datasets. Overall, EFP shows better performance than FP. The adaptive thresholding has the lowest accuracy of 93.61% in the mobile phone dataset, 97% in the Drishti-GS dataset, and 86.67% in the HFS dataset. The unsuccessful cases of adaptive thresholding are due to uneven illumination. The unsuccessful cases of FP and EFP are due to an incomplete vessel network and a faint OD in a brighter background.

Table 1: *Descriptions of each dataset and accuracy comparison of OD Localization.*

Datasets	Device and Total Images	OD Localization Methods			
		EM	EFP	FP	Adaptive Thresholding
Mobile Phone	iPhone Camera (94)	**100.00**	98.89	95.74	93.61
Drishti-GS	Standard Fundus Camera (101)	**100.00**	100.00	99.00	97.00
HFS	Canon CR-1 Fundus Camera (30)	**100.00**	100.00	90.00	86.67

4.2 OD and OC Segmentation

The OD and OC segmentations are done by using ADI-GVF snakes with the initial contour set to a circle that is centered at the OD returned by EM, with a radius equal to one-third of the width of the retina. We compared the segmentation results against three state-ot-the-art methods: region growing [26], watershed transformation [27], and traditional GVF [24]. The performance is evaluated by calculating the precision, recall, and F-score. The precision estimates the correctness of the algorithm's segmented region. The recall estimates the success rate of getting the ground truth region. The F-score measures the overall performance of the algorithm. The formulas are given in Equations (10) (11) and (12).

$$\text{Precision} = \left(\frac{TP}{TP+FP}\right) \tag{10}$$

$$\text{Recall} = \left(\frac{TP}{TP+FN}\right) \tag{11}$$

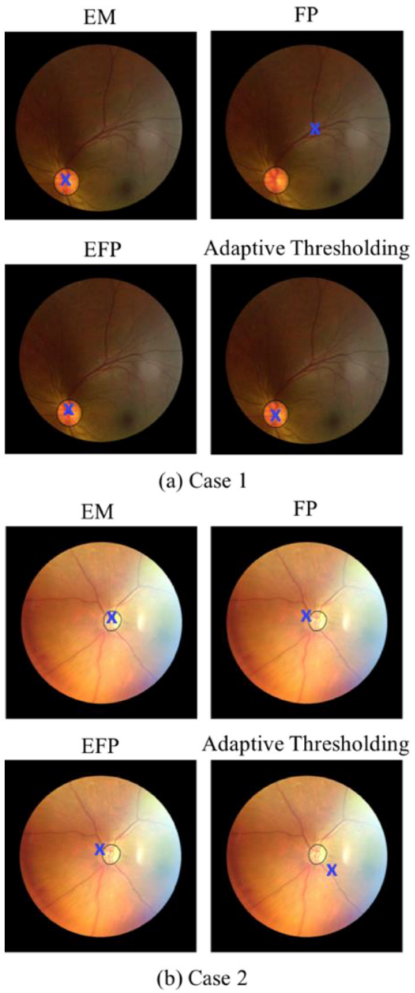

Fig.12: *Selected cases of OD localization.*

$$\text{F-measure} = 2 \times \left(\frac{precision \times recall}{precision + recall} \right) \quad (12)$$

TP, FP, TN, and FN are the numbers of true positive, false positive, true negative, and false negative pixels, respectively.

Fig. 13 illustrates the OD segmentation results for the mobile phone dataset from all compared methods. The ADI-GVF significantly outperforms other techniques. Under-segmentation often occurs when using region growing and traditional GVF. Those methods normally segment only the OC region, which is the brightest area in the OD. Watershed transformation often encounters an over-segmentation problem due to the low contrast between the retinal background and the OD.

Fig. 14 illustrates the OC segmentation results of the mobile phone dataset. ADI-GVF outperforms the other compared techniques. Region growing suffers from an over-segmentation problem. Watershed transformation and the traditional GVF have both over-segmentation and under-segmentation problems.

Table 2 shows the quantitative performance of the OD and OC segmentation in the mobile phone dataset. The ADI-GVF method achieves the highest recall and F-measure for OD segmentation, compared to the other approaches. It underperforms the traditional GVF about 5.14% in terms of precision. However, the ADI-GVF significantly outperforms all other compared methods for OC segmentation. The recall of segmentation of the ADI-GVF is as high as 88.05% for the OD and 82.27% for the OC. For precision, the ADI-GVF performs as high as 80.04% and 77.74% for the OD and OC, respectively.

Table 2: *Comparison of OD and OC segmentation accuracies for the Mobile Phone Dataset using ADI-GVF, region growing, watershed transformation, and traditional GVF.*

Methods	OD			OC		
	Recall	*Precision*	*F-Measure*	*Recall*	*Precision*	*F-Measure*
ADI-GVF	**88.50**	80.04	**84.06**	**82.27**	**77.74**	**79.94**
Region Growing	68.50	78.59	73.20	75.38	65.19	69.92
Watershed Transformation	87.78	67.89	76.56	60.03	73.51	66.09
GVF	75.03	**85.18**	79.78	79.43	75.83	77.59

Tables 3 and 4 show the quantitative performances of the OD and OC segmentation obtained from the Drishti-GS and HFS datasets, respectively. For the Drishti-GS dataset, the ADI-GVF underperforms the traditional GVF in terms of recall for both OD and OC segmentation, and it underperforms the region growing in terms of precision for OD segmentation. However, GVF and the region growing suffer from under-segmentation. Most cases of watershed transformation still encounter over-segmentation in the

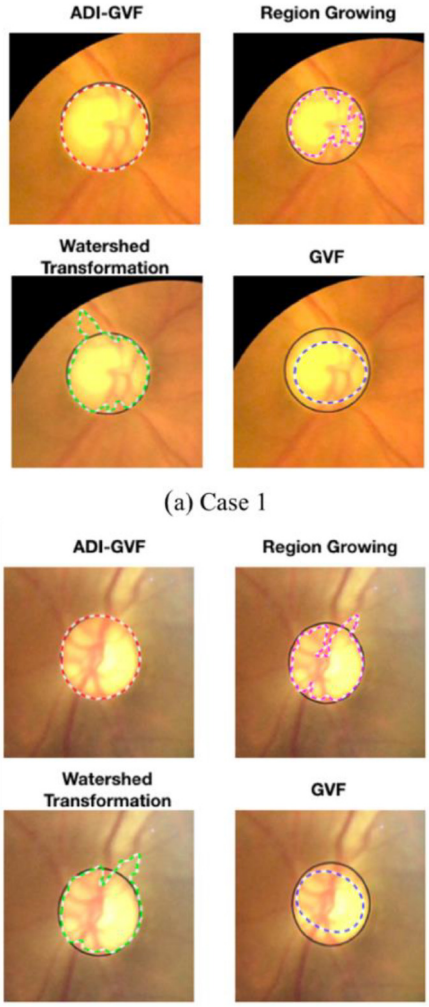

Fig.13: *Example results of OD Segmentation for the Mobile Phone Dataset from ADI-GVF, region growing, watershed transformation, and traditional GVF for two different cases. The black contour shows the ground truth of the OD boundary. The dotted contour represents the results from each approach.*

OD and OC. The overall performance of the ADI-GVF is the best. It achieves the highest F-score rate of 81.57% for the OD and 82.05% for the OC. The results of the OD and OC segmentation from the Drishti-GS dataset are shown in Fig.15. and Fig.17, respectively.

For the HFS dataset, the most images have uneven illumination around the OD boundary. All methods encounter an over-segmentation. However, ADI-GVF still provides the highest precision rate. The watershed transformation yields the lowest precision rate of 58.27%. Fig. 16 and Fig. 18 show the results of OD and OC segmentation for the HFS dataset.

In clinical applications, over-segmentation of the OD causes worse consequences than under-segmentation because it can yield a false negative.

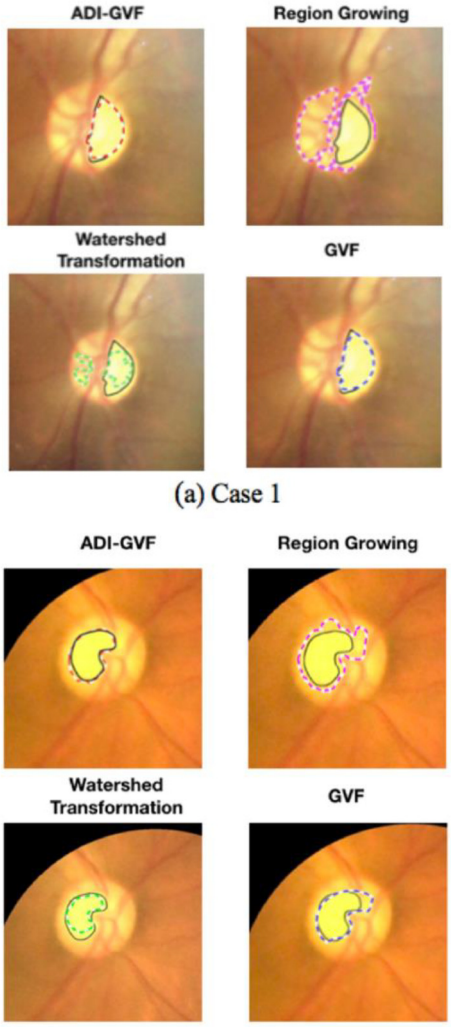

Fig.14: *Example of results of OC Segmentation for the Mobile Phone Dataset from ADI-GVF, region growing, watershed transformation, and traditional GVF for two different cases. The ground truth is drawn with the black contour. The dotted contour represents the results from each approach.*

Table 3: *Comparison of OD and OC segmentation accuracies of Drishti-GS Dataset performed by ADI-GVF, region growing, watershed transformation, and traditional GVF.*

Methods	OD			OC		
	Recall	*Precision*	*F-Measure*	*Recall*	*Precision*	*F-Measure*
ADI-GVF	78.97	84.35	**81.57**	81.10	**83.03**	**82.05**
Region Growing	59.39	**91.98**	72.18	77.52	79.04	78.27
Watershed Transformation	67.32	88.02	76.29	53.87	75.94	63.03
GVF	**89.81**	60.51	72.31	**92.05**	46.91	62.15

Table 4: *Comparison of OD and OC segmentation accuracies of HFS Dataset performed by ADI-GVF, region growing, watershed transformation, and traditional GVF.*

Methods	OD			OC		
	Recall	*Precision*	*F-Measure*	*Recall*	*Precision*	*F-Measure*
ADI-GVF	85.28	**72.57**	**78.41**	86.73	**75.01**	**80.45**
Region Growing	**87.51**	69.97	77.76	84.40	67.91	75.26
Watershed Transformation	83.95	63.91	72.57	91.43	47.54	62.55
GVF	72.23	58.27	64.50	**92.78**	50.62	65.50

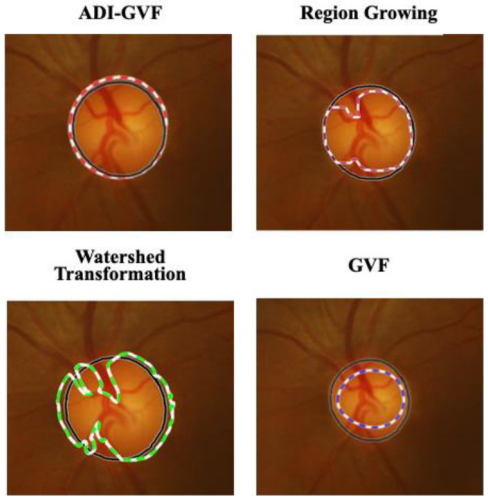

Fig.15: *Example of results of OD Segmentation in Drishti-GS Dataset from ADI-GVF, region growing, watershed transformation, and traditional GVF. The ground truth is drawn with the black contour.*

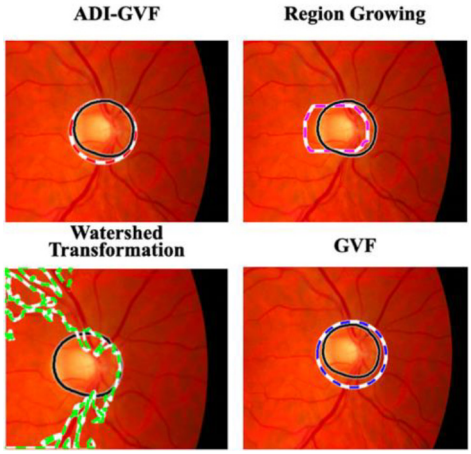

Fig.16: *Example of results of OD Segmentation in HFS Dataset from ADI-GVF, region growing, watershed transformation, and traditional GVF. The ground truth is drawn with the black contour.*

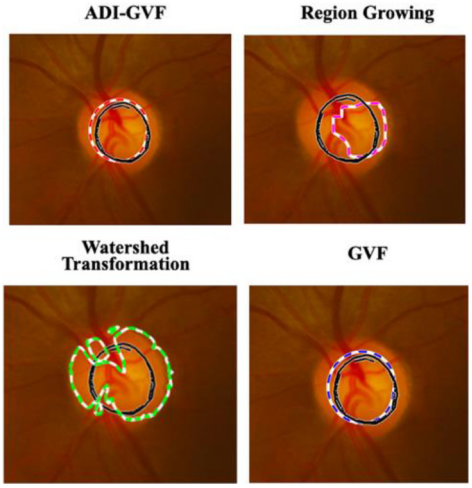

Fig.17: *Example of results of OC Segmentation in Drishti-GS Dataset from ADI-GVF, region growing, watershed transformation, and traditional GVF. The ground truth is drawn with the black contour.*

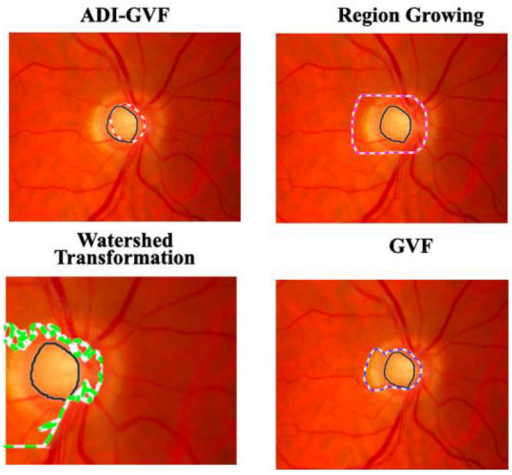

Fig.18: *Example of results of OC Segmentation in HFS Dataset from ADI-GVF, region growing, watershed transformation, and traditional GVF. The ground truth is drawn with the black contour.*

A false negative means that a (true) glaucoma patient does not meet an ophthalmologist. Overall, the ADI-GVF performs the best for a pre-screening application.

4.3 Glaucoma Classification

The performance of pre-screening for glaucoma is evaluated in terms of the true positive rate (TPR), the true negative rate (TNR), the false omission rate (FOR), and the false discovery rate (FDR). The formulas for these are shown in Equations (13), (14), (15), and (16), respectively. A comparison is shown in Table 4.

$$\text{TPR} = \left(\frac{TP}{TP+FN}\right) \tag{13}$$

$$\text{TNR} = \left(\frac{TN}{TN+FP}\right) \tag{14}$$

$$\text{FOR} = \left(\frac{FN}{FN+TN}\right) \tag{15}$$

$$\text{FDR} = \left(\frac{FP}{TP+FP}\right) \tag{16}$$

TP is the number of glaucoma images predicted correctly as glaucoma. TN is the number of healthy images predicted correctly as healthy images. FN is the number of glaucomatous images which are classified as healthy images. FP is the number of healthy images which are classified as glaucomatous images. Note that the TPR and TNR are also known as sensitivity and specificity. In clinical application, FOR is the most crucial as this can cause the most trouble when glaucomatous patients are predicted as healthy and consequently do not get treatment.

Table 5 represents the confusion matrix of the case prediction of glaucoma from our algorithm for the mobile phone dataset. There are 42 cases out of 45 classified correctly as glaucoma, and 46 cases out of 49 classified correctly as healthy. Our algorithm misclassified 3 glaucoma cases as healthy and 3 healthy cases as glaucoma. Only 6 images are classified incorrectly in this experiment.

Table 5: *Confusion Matrix of the prediction cases.*

Ground Truth		Predicted Class	
		Positive	Negative
	Positive (45)	42	3
	Negative (49)	3	46

Table 6 shows the performance for detecting glaucoma for the mobile phone dataset. Our proposed method achieves high sensitivity and specificity. The algorithm can classify 42 glaucomatous images and 46 healthy images correctly, resulting in a sensitivity of 93.33% and a specificity of 93.87%. In addition, the proposed method yields the lowest false omission rate (FOR) and false discovery rate (FDR) of 6.66% and 6.12%, respectively. For the misclassification rate, the false omission rate is significant in a clinical environment. Region growing and watershed transformation are worst choices for clinical assessment. We can conclude that our proposed method is the best for prescreening glaucoma. Moreover, this work improves the TPR, TNR, FOR, and FDR of our previous work of glaucoma prescreening that uses ADI-GVF for OD and OC segmentation and adaptive thresholding for

OD initialization [1] by 4.45%, 4.08%, 4.08%, and 4.44%, respectively.

Table 6: *Comparison of the glaucoma detection accuracy for the mobile phone dataset.*

Methods	Accuracy of glaucoma detection, %			
	TPR	TNR	FOR	FDR
ADI-GVF	**93.33**	**93.87**	**6.66**	**6.12**
Region growing	80.00	71.42	28.00	20.45
Watershed transformation	77.77	85.71	16.66	28.00
GVF	88.88	75.51	23.07	9.75

Tables 7 and 8 show the evaluation of glaucoma detection for the Drishi-GS and HFS datasets. Our method also yields the highest true positive rate of 95.71% and lowest false omission rate of 10.71% for the Drishi-GS dataset. As mentioned earlier, region growing and watershed transformation suffer an over-segmentation in the OC. That causes the high false discovery rate for the HFS dataset. From all datasets, it can be concluded that our method can be used in various kinds of retinal images, not only for the mobile phone dataset. In cases of insufficient quality images, ADI-GVF can work efficiently and provide higher performance than the other techniques. Additionally, the retinal images of the public datasets normally contain strong and clear blood vessel. EM can localize the OD centers correctly 100% of the time.

Table 7: *Comparison of the glaucoma detection accuracy for the Drishti-GS dataset.*

Methods	Accuracy of glaucoma detection, %			
	TPR	TNR	FOR	FDR
ADI-GVF	**95.71**	**80.64**	**10.71**	**8.21**
Region Growing	88.57	61.29	29.62	16.21
Watershed Transformation	97.14	51.61	11.11	18.07
GVF	92.85	54.83	22.72	17.72

Table 8: *Comparison of the glaucoma detection accuracy for the HFS dataset.*

Methods	Accuracy of glaucoma detection, %			
	TPR	TNR	FOR	FDR
ADI-GVF	**80.00**	**86.66**	**18.75**	**14.28**
Region Growing	66.66	26.66	55.55	52.38
Watershed Transformation	73.33	26.66	50.00	50.00
GVF	73.33	86.66	23.52	15.38

There are 6 images in the mobile phone dataset that the algorithm classified images incorrectly. The unsuccessful cases from all datasets are caused by two main issues: unsuccessful OC segmentation and unsuccessful OD localization. For unsuccessful OC segmentation, over-segmentation in a healthy case is usually the cause. The ADI-GVF algorithm over-segments the cup region because ranges of intensity of the OD and the OC are too close together. Thus, this causes the CDAR to be higher than the actual rate, resulting in a wrong prediction. The second cause is the under-segmentation of the OC in glaucoma cases due to a large region of blood vessels within the OC. The OC region is then segmented with a smaller size than the actual size. In some cases, the OC intensity is not uniform. Thus, when intensity histogram equalization is used, it can cause under-segmentation of the OC. In those cases, the system classifies those images as healthy. Examples of those problems in the OC are shown in Fig. 19.

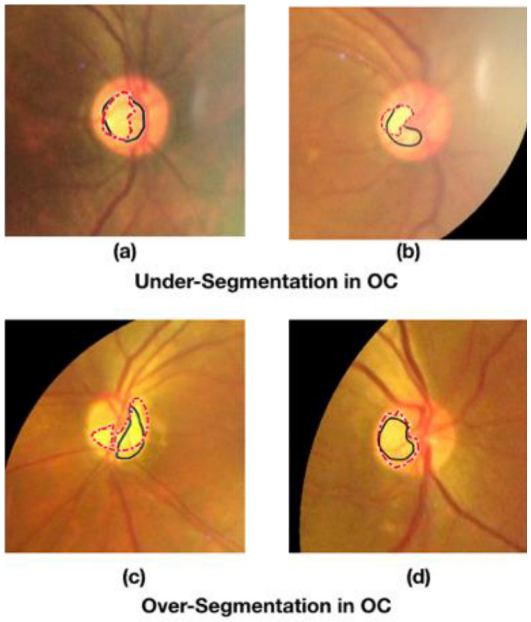

Fig.19: *Examples of unsuccessful OC segmentation. The black solid contour is the ground truth. The red dotted contour is the segmented OC from our algorithm.*

The last issue is a result of the OD locations. Fig. 20 illustrates an example of this problem. The blue cross symbols are the OD locations returned by the EM. The OD is located close to the rim of the OD, and the ADI-GVF method uses a circle with a radius equal to one third of the width of the retina as the initial contour. Thus, it starts with an initial contour that doesn't cover the OD region, resulting in a wrong final OD region. In those cases, it reports an incorrect prediction. We have tried to enlarge the initial curve to ensure that the curve covers the OD regions. However, we still cannot completely solve this problem. When the initial curve is larger, our method still does not work well due to uneven illumination of the background. For all of those problems,

we plan to investigate ways to solve and improve our work in the future.

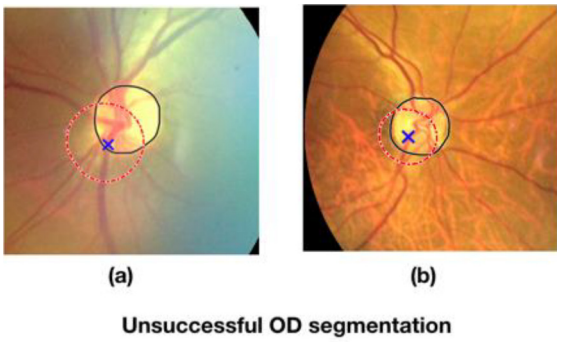

Fig.20: *Examples of unsuccessful OD segmentation due to an OD location too close to the rim of the OD.*

5. CONCLUSION

In this work, ADI-GVF snakes for image segmentation is combined with the exclusion method (EM) for localizing the OD. This was to enhance our previous work [1] for pre-screening glaucoma by using mobile phone retinal images. The EM works well for OD localization. It achieves 100% accuracy. Overall, ADI-GVF with EM yields great performance. For the mobile phone dataset, the ADI-GVF with the EM for OD localization is better than other segmentation techniques, including our previous work. The F-measures for OD and OC segmentation are 84.06% and 79.94%, respectively. The performance of glaucoma detection using our methods has the best TPR and TNR, which are 93.33% and 93.87%, respectively. Our new method has the lowest FOR rate of less than 6.66%. The TPR and TNR of glaucoma prescreening increase by 4.45% and 4.08% and the FOR and FDR decreases by 4.08% and 4.44% compared to those of our previous work [1] for the mobile phone dataset.

The proposed method achieves the best F-measure rates of 81.57% and 78.41% for the OD segmentation, and 82.05% and 80.45% for the OC segmentation using the standard datasets Drishi-GS and HFS respectively. In addition, it shows the best performance of glaucoma assessment for these datasets, obtaining the highest TPR, the highest TNR, the lowest FPR, and the lowest FOR rates. Our work has proven to work well for the standard datasets.

Our work could be improved and extended to segment other regions in retinal images such as fovea, macula, or exudates. Thus, it could be helpful in related ophthalmological applications. Our sub-algorithm, for example, ADI-GVF for segmentation of the optic disk and cup, can also be applied generally in the research area of object segmentation in a low contrast environment. The concept of EM for OD localization can be applied generally in the field of object localization based on pattern recognition from an object's edges.

References

[1] T. Ruennark et al., "Alternative deflation-inflation gradient vector flow snakes for prescreening glaucoma in mobile phone retinal images," in *Proceedings of the 23rd International Computer Science and Engineering Conference (ICSEC)*, 2019.

[2] H. A. Quigley and A. T. Broman, "The number of people with glaucoma worldwide in 2010 and 2020," *The British Journal of Ophthalmology*, vol.90, no.3, pp.262-267, 2006.

[3] World Health Organization, "Blindness and vision impairment," *Publication of Universal Eye Health: a global action plan 2014-2019*, accessed 1 October 2019.

[4] V. Kalpiyapan et al., "An automatic system to detect exudates in mobile-phone fundus images for DR-pre-screening," in *Proceedings of the 13th International Conference on Knowledge, Information and Creativity Support System (KICSS)*, pp. 287-292, 2018.

[5] R. Besenczi et al., "Automatic optic disc and optic cup detection in retinal images acquired by mobile phone," *9th International Symposium on Image and Signal Processing and Analysis (ISPA)*, pp.193-198, 2015.

[6] A. M. Jose and A. A. Balakrishnan, "A novel method for glaucoma detection using optic disc and cup segmentation in digital fundus images," *International Conference on Circuits, Power and Computing Technologies (ICCPCT)*, pp.1-5, 2015.

[7] A. Almazroa, R. Burman, K. Raahemifar and V. Lakshminarayanan, "Optic disc and optic cup segmentation methodologies for glaucoma image detection: A survey," *Journal of Ophthalmology*, vol.2015, 2015.

[8] R. L. Weisman et al., "Vertical elongation of the optic cup in glaucoma," *Trans AM Acad Ophthalmol Otolaryngol*, vol.77, no.2, pp.157-161, 1973.

[9] J. C. Morrison, W. O. Cepurna and E. C. Johnson, "Pathophysiology of human glaucomatous optic nerve damage: insights from rodent models of glaucoma," *Experimental Eye Research*, vol.93, no.2, pp.156-164, 2011.

[10] N. Harizman et al., "The ISNT rule and differentiation of normal from glaucomatous eyes," *Arch Ophthalmol*, vol.124, no.11, pp.1579-1583, 2006.

[11] M. Lalonde, M. Beaulieu and L. Gagnon, "Fast and robust optic disc detection using pyramidal decomposition and Hausdroff-based template matching," in *IEEE Transactions on Medical Imaging*, vol.20, no.11, pp.1193-1200, 2001.

[12] A. Sopharak, K. T. Nwe, Y. A. Moe and M. N. Dailey, "Automatic exudate detection with a naïve Bayes classifier," *International Conference*

on Embedded Systems and Intelligent Technology, pp. 139-142, 2008.

[13] P.C. Siddalingaswamy and P.K. Gopalakrishna, "Automatic localization and boundary detection of optic disc using implicit active contours," *International Journal of Computer Applications*, vol. 1, no.7, 2010.

[14] A. Hoover and M. Goldbaum, "Locating the optic nerve in a retinal image using the fuzzy convergence of the blood vessels," in *IEEE Transactions on Medical Imaging*, vol. 22, no. 8, pp.951-958, 2003.

[15] N. Muangnak, P. Aimmanee and S. S. Makhanov, "Vessel transform for automatic optic disk detection in retinal images," *IET Image Processing*, vol. 9, issue 9, pp. 743-750, 2015.

[16] N. Muangnak, P. Aimmanee and S. S. Makhanov, "Automatic optic disk detection in retinal images using hybrid vessel phase portrait analysis," *Medical, Biological Engineering and Computing*, vol. 56, issue 4, pp. 583-598, 2018.

[17] A. E. Mahfouz and A. S. Fahmy, "Ultrafast localization of the optic disc using dimensionality reduction of the search space," *International Conference on Medical Image Computing and Computer-Assisted Intervention (MICCAI)*, pp. 985-992, 2009.

[18] A. E. Mahfouz and A. S. Fahmy, "Fast localization of the optic disc using projection of image features," *IEEE Transcations on Image Processing*, pp.3285-3289, 2010.

[19] T. T. Khaing and P. Aimmanee, "Optic disk segmentation in retinal images using active contour model based on extended feature projection," in *Proceedings of the 8th International Conference of Information and Communication Technology for Embedded Systems (IC-ICTES)*, 2017.

[20] G. D. Joshi, J. Sivaswamy and S. R. Krishnadas, "Optic disk and cup segmentation from monocular color retinal images for glaucoma assessment," in *IEEE Transactions on Medical Imaging*, vol. 30, no. 6, pp.1192-1205, 2011.

[21] M. J. Cox and I. C. J. Wood, "Computer-assisted optic nerve head assessment," *Ophthalmic Physiol. Opt.*, vol. 11, no. 1, pp. 27–35, Jan. 1991.

[22] S. Karkuzhali and D. Manimegalai, "Computational intelligence-based decision support system for glaucoma detection," *Biomedical Research*, Vol. 28. No. 11, pp.4737-4748, 2017.

[23] S. Giraddi, J. Pujari and P. S. Hiremath, "Optic disc detection using geometric properties and GVF snake," *2017 1st International Conference on Intelligent Systems and Information Management (ICISIM)*, pp.141-146, 2017.

[24] D. E. Kusumandari, A. Munandar and G. G. Redhyka, "The comparison of GVF snake active contour method and ellipse fit in optic disc detection for glaucoma diagnosis," *2015 International Conference on Automation, Cognitive Science, Optics, Micro Electro-Mechanical System, and Information Technology (ICACOMIT)*, pp.123-126, 2015.

[25] TM. Khan, M. Mehmood, SS. Naqvi, MFU. Butt, "A region growing and local adaptive thresholding-based optic disc detection," *PLoS ONE* 15(1): e0227566. `https://doi.org/10.1371/journal.pone.0227566`.

[26] P. Das, S.R. Nirmala and J.P. Medhi, "Diagnosis of glaucoma using CDR and NRR area in retina images," *Network Modelling Analysis in Health Informatics and Bioinformatic*, vol. 5, No. 3, 2015.

[27] R. Preethi Rajaiah, R. John Britto, "Optic Disc Boundary Detection and Cup Segmentation for Prediction of Glaucoma," *International Journal of Science, Engineering and Technology Research (IJSETR)*, vol. 3, Issue 10, October 2014.

[28] W. K. Wong, J. Liu, J.H. Lim, H. li and T.Y. Wong, "Automated detection of kinks from blood vessels for optic cup segmentation in retinal images," *Proceedings of SPIE - The International Society for Optical Engineering*, vol. 7260, 2009.

[29] X. Chen et al., "Glaucoma detection based on deep convolutional neural network," *2015 3712th Annual International Conference of the IEEE Engineering in Medicine and Biology Society (EMBC)*, pp.715-718, 2015.

[30] X. Chen et al., "Automatic feature learning for glaucoma detection based on deep learning," *International Conference on Medical Image Computing and Computer-Assisted Intervention (MICCAI 2015)*, Springer, 2015.

[31] L. Li, M. Xu, X. Wang, L. Jiang and H. Liu, "Attention based glaucoma detection: a large-scale database and CNN model," *2019 IEEE/CVF Conference on Computer Vision and Pattern Recognition (CVPR)*, Long Beach, CA, USA, pp. 10563-10572, 2019.

[32] T. T. Khaing and P. Aimmanee, "Optic disk localization in retinal image using exclusion method," in *Proceedings of the 12th international conference on Knowledge, Information and Creativity Support System (KICSS)*, 2017.

[33] I. Marjanovic, "The optic nerve in glaucoma," *The Mystery of Glaucoma, Tomaš Kubena, IntechOpen*, Available: `https://www.intechopen.com/books/the-mystery-of-glaucoma/the-optic-nerve-in-glaucoma.`, 2011.

[34] V. David. "Volk INview — iPhone Fundus camera.," *Volk- INview — iPhone Fundus camera*, `http://volk.com/index.php/volk-products/ophthalmic-cameras/volk-inview.html.`, accessed 1 August 2018.

[35] J. Sivaswamy, S.R. Krishnadas, A. Chakravarty, G.D. Joshi , U. A. Syed and T.A. Syed, "A Comprehensive Retinal Image Dataset for the Assess-

ment of Glaucoma from the Optic Nerve Head Analysis," *JSM Biomed Imaging Data Papers*, vol.2(1): 1004, 2015.

[36] A. Budai, R. Bock, A. Maier, J. Hornegger and G. Michelson, "Robust Vessel Segmentation in Fundus Images," *International Journal of Biomedical Imaging*, vol. 2013, 2013.

[37] A. Scarpa, "D-eye, retinal screening system for smartphones," `https://www.d-eyecare.com`, 2014, accessed 1 August 2018.

[38] A. Bastawrous, "Peek vision," `https://www.peekvision.org`, accessed 9 July 2019.

[39] W. Allyn, "Retinal cameras, Welch Allyn iExaminer," `https://www.welchallyn.com`, 2019, accessed 21 November 2019.

Tin Tin Khaing is a double doctoral degree candidate at Thammasat University, Thailand and Chiba University, Japan. She received her M.S. in Engineering and Technology from Thammasat University. Her research area is medical image processing.

Thayanee Ruennark is currently a master degree candidate in Engineering and Technology at Thammasat University, Thailand. Her research interest is medical image processing.

Pakinee Aimmanee is an Associate Professor at Thammasat University, Thailand. Her background is Applied Mathematics. She currently researches in the areas of medical image processing, information retrieval, and audio watermarking.

Stanislav Makhanov is a Full Professor and a Head of Center of Excellence in Biomedical Engineering of Thammasat University, Thailand. His MS and Ph.D. degrees are in Applied Mathematics from Moscow State University and Computing Center of the Russian Academy of Science. His research areas are medical image processing, robotics, pattern recognition and grid generation.

Navapol Kanchanaranya is an Associate Professor at the Department of Ophthalmology, Faculty of Medicine, Thammasat University, Thailand. His research interests include biomedical optical imaging and medical image processing.